MATERIALS SCIENCE

Bright circularly polarized photoluminescence in chiral layered hybrid lead-halide perovskites

Shangpu Liu[1,2], Mikaël Kepenekian[3], Stanislav Bodnar[1,2], Sascha Feldmann[4], Markus W. Heindl[1,2], Natalie Fehn[5], Jonathan Zerhoch[1,2], Andrii Shcherbakov[1,2], Alexander Pöthig[5], Yang Li[6,7], Ulrich W. Paetzold[6,7], Aras Kartouzian[5], Ian D. Sharp[2], Claudine Katan[3], Jacky Even[8], Felix Deschler[1]*

Hybrid perovskite semiconductor materials are predicted to lock chirality into place and encode asymmetry into their electronic states, while softness of their crystal lattice accommodates lattice strain to maintain high crystal quality with low defect densities, necessary for high luminescence yields. We report photoluminescence quantum efficiencies as high as 39% and degrees of circularly polarized photoluminescence of up to 52%, at room temperature, in the chiral layered hybrid lead-halide perovskites (R/S/Rac)-3BrMBA$_2$PbI$_4$ [3BrMBA = 1-(3-bromphenyl)-ethylamine]. Using transient chiroptical spectroscopy, we explain the excellent photoluminescence yields from suppression of nonradiative loss channels and high rates of radiative recombination. We further find that photoexcitations show polarization lifetimes that exceed the time scales of radiative decays, which rationalize the high degrees of polarized luminescence. Our findings pave the way toward high-performance solution-processed photonic systems for chiroptical applications and chiral-spintronic logic at room temperature.

INTRODUCTION

Chiral semiconductors offer fascinating opportunities for the design of electronic state dissymmetry and spin-orbit coupling (SOC), which underpin exciting spintronic and optoelectronic applications, such as circular polarized light-emitting diodes (LEDs) or chirality-induced spin selectivity (CISS) spin-filters (1–5). The generation of bright circularly polarized luminescence (CPL) is a long-standing objective in material science (6–10). The required chiral, distorted crystal structures may lead to defects and nonradiative losses in some inorganic materials (11, 12), while the brightness of structurally versatile, chiral molecular semiconductors suffer from populations of dark triplet excitons. CISS effects enable selective spin injection into materials in the absence of magnetic fields or external spin-selective layers, thereby greatly expanding approaches to advanced spintronic applications (5, 13, 14). Despite this technological and scientific interest, inducing large degrees of structural chirality typically limits opto-electronic performance in current material systems.

Hybrid metal-halide perovskite (HMHP) semiconductors are attractive optoelectronic materials, which hold promise for application as solar cells, photodetectors, lasers, and perovskite LEDs (PeLEDs). The class of two-dimensional (2D) layered HMHPs shows strong quantum confinement and excitonic states, which

have garnered intense research attention (15). Furthermore, 2D HMHPs feature compositional and structural diversity, which make them attractive platforms for multifunctional materials exhibiting, for example, piezoelectricity, ferroelectricity, magnetic properties, and chirality (5, 16–19). However, it remains a substantial challenge to preserve the efficient optical properties of HMHPs, while also introducing additional functionalities from large and/or geometrically complicated organic molecules, which could limit their practical applications.

In chiral layered HMHPs, the use of chiral molecules as organic cations transfers chirality into the metal-halide sublattice (20–24), which forms chiral crystal structures with highly distorted octahedral frameworks of the Sohncke space groups. Such structures have shown chiroptical properties, including circular dichroism (CD) and circularly polarized photoluminescence (CPL) (17, 20, 25). HMHPs further show strong SOC, large Rashba splitting, and long polarization lifetimes (26), which make them suitable materials for spintronic applications. Applications based on bright chiral perovskites would benefit from intrinsic characteristics of spin state manipulation and readout, such as low energy consumption and high memory density (13). Chiral perovskites with efficient carrier spin polarization due to their asymmetric chiral structures have already successfully led to spin-LEDs or circularly polarized light detectors (5, 27). However, layered 2D HMHPs usually exhibit low photoluminescence quantum efficiency (PLQE) values at room temperature, and recent work on chiral layered HMHPs found that using chiral organic cations further decreased the PLQE (20), indicating strong losses from nonradiative recombination.

Here, we report on the structural and chiroptical properties of the, to the best of our knowledge, previously unknown chiral layered HMHP (R/S)-3BrMBA$_2$PbI$_4$ [3BrMBA = 1-(3-bromphenyl)-ethylamine]. We use single-crystal x-ray diffraction (SCXRD) to resolve chiral crystal structures. PL quantum efficiency

[1]Physikalisch-Chemisches Institut, Universität Heidelberg, Im Neuenheimer Feld 229, 69120 Heidelberg, Germany. [2]Walter Schottky Institute and Physics Department, Technical University of Munich, Am Coulombwall 4, 85748 Garching, Germany. [3]Univ Rennes, ENSCR, INSA Rennes, CNRS, ISCR (Institut des Sciences Chimiques de Rennes)—UMR 6226, F-35000 Rennes, France. [4]Rowland Institute, Harvard University, Cambridge, MA 02142, USA. [5]Catalysis Research Center and Chemistry Department, Technical University of Munich, Lichtenbergstraße 4, 85748 Garching, Germany. [6]Institute of Microstructure Technology, Karlsruhe Institute of Technology, 76344 Eggenstein-Leopoldshafen, Germany. [7]Light Technology Institute, Karlsruhe Institute of Technology, 76131 Karlsruhe, Germany. [8]Univ Rennes, INSA Rennes, CNRS, Institut FOTON—UMR 6082, F-35000 Rennes, France.
*Corresponding author. Email: deschler@uni-heidelberg.de

measurements show remarkably high values of up to 39%, at room temperature. Optical measurements show a large degree of CPL of up to ~50% upon linear excitation and strong CD signals at the absorption band position. We study excitation dynamics and decay channels with transient absorption (TA) spectroscopy, which show fast decays that indicate efficient radiative recombination. Circularly polarized TA (CTA) measurements further confirm that polarization lifetimes are far longer than the radiative PL lifetimes, which results in the high degree of CPL.

To the best of our knowledge, no bulk semiconductor has shown such high PLQE and degree of PL polarization at room temperature simultaneously (table S1) (16, 20, 25, 28–33). Our demonstration of how organic cation engineering can be used for fabrication of high-performance chiral layered HMHPs opens up exciting strategies for hybrid chiral semiconductors and opportunities for the design of chiroptical photonic and spintronic applications.

RESULTS AND DISCUSSION

Chirality transfer in the (S/R)-3BrMBA$_2$PbI$_4$ crystal lattice

We prepared lead-halide perovskite single crystals via hydrothermal synthesis with controlled cooling (see Materials and Methods for details). SCXRD was performed to obtain the crystal structures for chiral (S/R) and racemic (Rac)-3BrMBA$_2$PbI$_4$ (Fig. 1, A and B). Both materials acquire a 2D layered perovskite structure in which inorganic corner-sharing [PbI$_4$]$^{2-}$ octahedra monolayers are sandwiched between two organic amine layers (see detailed crystallographic information in table S2). Single-crystal structure analysis confirms that introducing the chiral organic cations (Fig. 1C) into the 2D perovskite framework results in the formation of a chiral crystal structure for (S)-3BrMBA$_2$PbI$_4$, which crystallizes in the non-centrosymmetric Sohncke space group $P\,2_1$. In contrast, Rac-3BrMBA$_2$PbI$_4$ crystallizes in the centrosymmetric $P\,2_1/c$ space group. We take this as evidence for chirality transfer from chiral organic cations to the perovskite network. Furthermore, analysis

of the bond length distortion index (D) and bond angle variance degree (σ^2) quantifies the average distortion degree of the perovskite octahedron (detailed calculations in table S3) (24, 34), which both would be zero with perfect O_h symmetry. Compared to the racemic sample ($D = 0.006$, $\sigma^2 = 20.87$), chiral (S)-3BrMBA$_2$PbI$_4$ shows a twofold increase of the distortion index D (0.012) and a higher angle variance value of 31.91. These are larger values compared to other reported chiral 2D lead-iodide perovskites, ~20 for (S)-MBA$_2$PbI$_4$, and ~13 for (S)-4BrMBA$_2$PbI$_4$ (16, 35), which may lead to high polarization results in chiral 3BrMBA$_2$PbI$_4$. We further consider that the relevant structural descriptor for the Rashba effect in chiral structures is the in-plane interoctahedral distortion angle β (Pb-I-Pb bond angle) disparity $\Delta\beta = \beta_{max} - \beta_{min}$ (vide infra) (35). The β angle is equal to 149.7° in the crystallographic structure of Rac-3BrMBA$_2$PbI$_4$. While β does not have a single value in chiral structures, the minimum value $\beta_{min} = 141.3°$ is smaller than the value in the racemic structure (table S3). This difference is indicative of larger local distortions in the structure of (S)-3BrMBA$_2$PbI$_4$. We find a minimum value of $\beta_{min} = 141.3°$ for the in-plane interoctahedral distortion angle β in the crystallographic structure of (S)-3BrMBA$_2$PbI$_4$, while a larger value $\beta_{min} = 148.2°$ is obtained for the crystallographic structure of (S)-4BrMBA$_2$PbI$_4$.

We fabricated polycrystalline thin films by spin coating for optical spectroscopy experiments. The precursor solution was prepared by dissolving the as-synthesized perovskite crystals or powders in N,N'-dimethylformamide (DMF). The XRD data from perovskite thin films agree with the simulated patterns from SCXRD (Fig. 1D), indicating successful transfer of single-crystal structures to thin films. Experimental XRD further confirms that both (R)- and (S)-3BrMBA$_2$PbI$_4$ have similar crystal structures with comparable diffraction patterns (Fig. 1D), as discussed in a previous work (23). Compared with the enantiomeric chiral variants, Rac-3BrMBA$_2$PbI$_4$ shows a similar diffraction pattern, except for the disappearance of (025) and (135) reflections at the diffractions of 33° and 42°. We checked these two missing reflexes in SCXRD
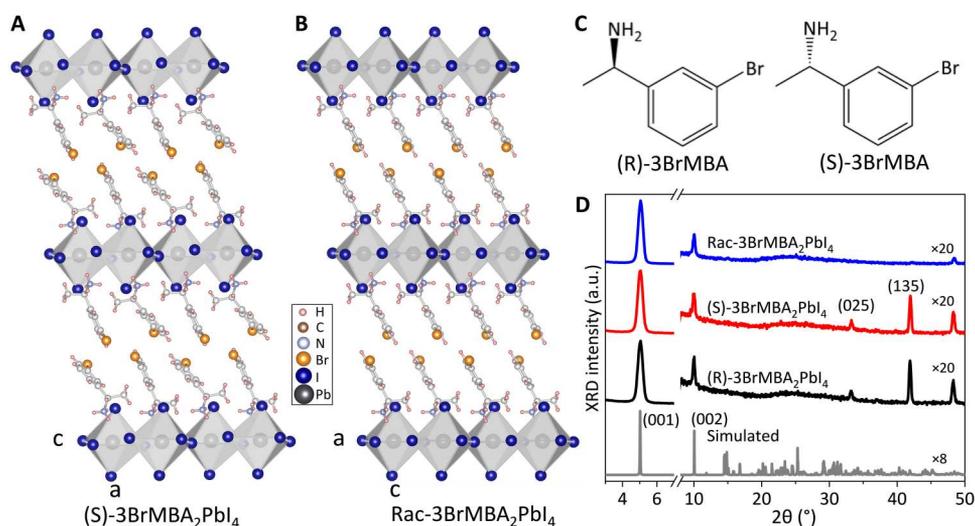
Fig. 1. Structure of layered (S/Rac)-3BrMBA$_2$PbI$_4$ perovskites. (**A** and **B**) Crystal structure of (S)-3BrMBA$_2$PbI$_4$ and Rac-3BrMBA$_2$PbI$_4$ single-crystal structures. (**C**) Chemical structures of chiral organic enantiomers (R/S)-3BrMBA. (**D**) XRD patterns of chiral (R/S)-3BrMBA$_2$PbI$_4$ and Rac-3BrMBA$_2$PbI$_4$ thin films. Compared with racemic cations, chiral spacer cations (R/S)-3BrMBA induce structure distortions in the orientation of organic spacers, as well as in inorganic layers, resulting in chiral crystal lattices. a.u., arbitrary units.

results and found both of them to exist in chiral and racemic single crystals. Thus, we tentatively attribute their disappearance in racemic spin-coated film samples to recrystallization processes from single crystals to thin films, which exhibit preferred orientations. The diffraction patterns simulated from SCXRD results also show that there are clear peak shifts between chiral perovskite and racemic samples (fig. S1), indicating that the chirality changes and structure distortions mainly occur along (001) and (110) planes.

Steady-state chiroptical characterization

Steady-state linear absorption spectra of chiral (R)- and (S)-$3BrMBA_2PbI_4$ show an excitonic band at 488 nm, while racemic samples have a red-shifted excitonic resonance at 500 nm (Fig. 2A). Compared to reported chiral perovskites (24, 25, 34), this blue shift (~60 meV) between the chiral and their racemic analogs reflects the stronger structural distortion induced by chiral organic cations in our chiral perovskites. We then performed CD measurements on the chiral variants, which indicate that chiral structural features are transferred to the electronic states of (R)- and (S)-$3BrMBA_2PbI_4$, with clear opposite CD signals from 300 to 550 nm, which are not found for racemic samples (Fig. 2B). The similar trend was also found in their absorption anisotropy factor plots (fig. S2). The highest CD values of our chiral perovskites are located at the excitonic absorption peak position. This result agrees with the Neumann-Curie principle (36, 37), which predicts that our perovskite materials, which have chiral crystal structures and belong to Sohncke space groups, will exhibit chiral optical properties.

Having established the optical absorption characteristics, we performed PL spectroscopy measurements on our chiral and racemic perovskite thin films at room temperature (Fig. 2C). Chiral (R/S)-$3BrMBA_2PbI_4$ show similar PL features, with a sharp excitonic emission at ~496 nm, while the PL peak of Rac-$3BrMBA_2PbI_4$ is located at ~508 nm. All peaks are slightly (~40 meV) red-shifted compared to their corresponding absorption spectra. We attribute this effect to different values of Stokes shift, which is likely to differ for materials with different levels of lattice strain and has been widely observed and reported in metal-halide perovskite materials (38). The signal from (R)- and (S)-$3BrMBA_2PbI_4$ films (Fig. 2C) is comparable, while the PL intensity of Rac-$3BrMBA_2PbI_4$ sample is higher than the chiral samples. Upon 405-nm excitation with a fluence of 132.7 mW/cm^2 (details in Materials and Methods), we find a PLQE value of 19% (±5%) for chiral 2D perovskite thin films and a value of 39% (±4%) for single crystals. This high PLQE value indicates strong radiative recombination channels in our chiral 2D perovskites, which is an unexpected result for chiral 2D perovskites with symmetry-broken structures (20).

We then performed circularly polarized PL measurements at room temperature on flat single-crystal samples (fig. S3). To avoid the injection of polarized states from circularly polarized excitation, we photoexcited the samples with a linearly polarized laser at a wavelength of 405 nm, passed the generated emission through a quarter waveplate, a Wollaston prism, to separate right- and left-handed circularly polarized emission, a 45° linear polarizer and into the spectrometer/camera system. Right-handed and left-handed emissions were simultaneously collected in different regions of the camera array (details in Materials and Methods). We collected CPL spectra for (R)-, Rac-, and (S)-$3BrMBA_2PbI_4$
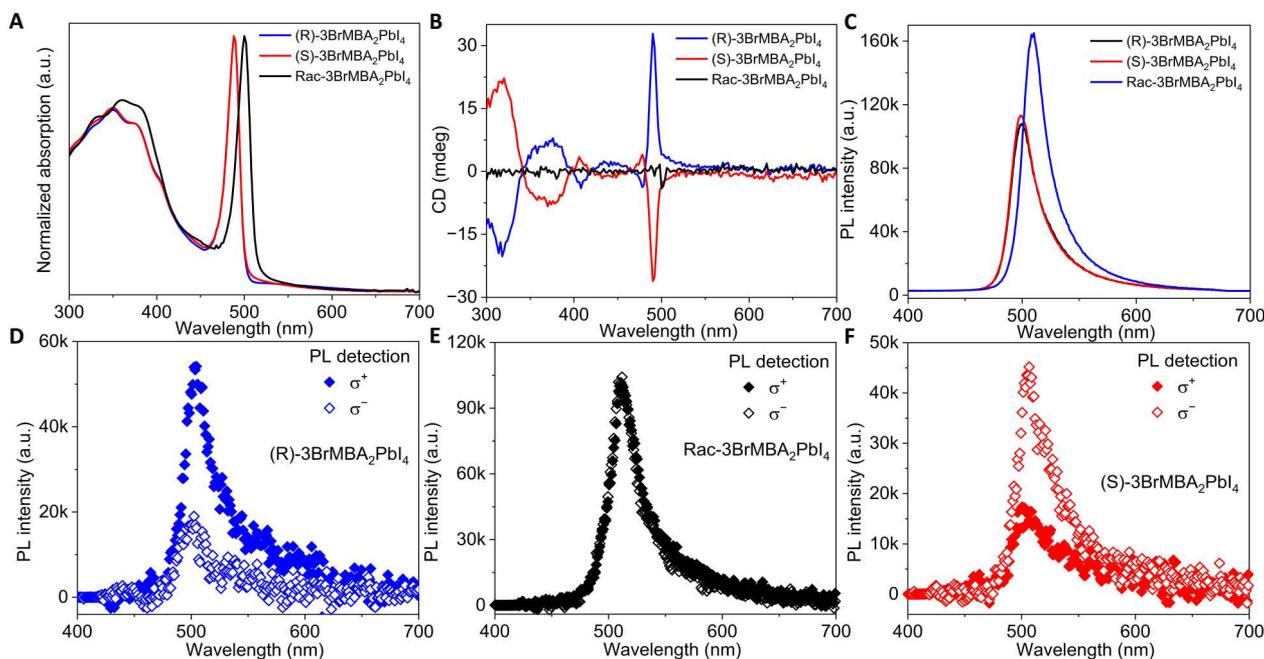
Fig. 2. Comparison of optical properties for chiral (R/S)-3BrMBA$_2$PbI$_4$ and Rac-3BrMBA$_2$PbI$_4$. (**A**) Linear absorption, (**B**) CD, and (**C**) linear PL spectra of chiral layered Ruddlesden-Popper hybrid perovskite thin films. (**D** to **F**) Circularly polarized PL (CPL) spectra of (R/S)-3BrMBA$_2$PbI$_4$ and Rac-3BrMBA$_2$PbI$_4$ single crystals at room temperature. Chiral (R)- and (S)-3BrMBA$_2$PbI$_4$ show similar linear optical features but with opposite CD signals, while the racemic sample shows no CD signals and is characterized by red-shifted absorption and PL bands. CPL results were obtained under linear excitation at 405 nm, and σ$^+$ and σ$^-$ signals were detected simultaneously on different regions of the detector. Chiral (R) and (S) crystals exhibit opposite CPL signals, while racemic samples show identical σ$^+$ and σ$^-$ signals, confirming that crystal chirality induces chiroptical properties.

single-crystal samples (Fig. 2, D, E, and F), where each spectrum plot is the average result from five different spots on the crystal. We find stark differences between the spectra of right-handed and left-handed detection channels. (R)- and (S)-3BrMBA$_2$PbI$_4$ crystals show opposite intensity differences for left/right-handed CPL, in agreement with their CD absorption signals. In contrast, Rac-3BrMBA$_2$PbI$_4$ crystals show no detectable difference in PL intensity between right-handed and left-handed detection channels. We also show the PL intensity difference between right-handed and left-handed detections for all three samples (fig. S4). We find that the intensity differences for chiral (R) and (S) samples cover a broad wavelength range from 480 to 600 nm. Such broad CPL signals are also found in other chiral perovskites (16, 28, 39, 40), which may derive from strong electron-phonon interaction in low-dimensional perovskites. Quantitatively, the degrees of polarization of CPL can be expressed as

$$P_{CPL} = \frac{I_{\sigma^+} - I_{\sigma^-}}{I_{\sigma^+} + I_{\sigma^-}}$$

where I_{σ^+} and I_{σ^-} are the integrated PL spectral intensities with right-handed and left-handed detectors, respectively. The calculated P_{CPL} of chiral (R)- and (S)-3BrMBA$_2$PbI$_4$ crystals at room temperature are ~52 and ~34%, respectively, which is five times larger than previously reported best values for the chiral 2D perovskite (R)-4BrMBA$_2$PbI$_4$ (16). We postulate that the different P_{CPL} values for (R) and (S) samples may be caused by the different amounts of chiral enantiomers of these chiral crystals, which may relate to the ratio of enantiomers (~98.0%) inside chiral organic precursors that we used to grow single-crystal samples. We find support for this hypothesis from the Flack parameter in our crystal refinement, which indicates enantiomeric purity around 95%. No detectable

CPL polarization was found in our setup for the MAPbBr$_3$ or Rac-3BrMBA$_2$PbI$_4$ reference samples (fig. S5), as expected. Notably, the full width at half maximum (FWHM) of the CPL spectra is ~150 meV for all three crystal samples, which is a slightly larger value than that of corresponding linear PL spectra (~140 meV) collected from spin-coated thin films. We attribute this small difference to weak emission from a dark state below bandgap, which is more readily detected in single-crystal samples (fig. S6) (41). We also extracted the g_{abs} and g_{lum} at band edge positions from our CD and CPL measurements. We find that the g_{abs} value (~0.0004) is much smaller than the obtained g_{lum} value (~0.95; details of calculations are in the Supplementary Materials), which provides further evidence that the CPL result does not exclusively originate in the preferred absorption of one kind of circular polarized light, as demonstrated in the CD measurements.

We further compared the CPL results between linear excitations and circularly polarized excitations (fig. S7). Under right-handed excitation, compared to linear excitation, we observed a slight increase of PL polarizations for chiral (R) samples and a small decrease of PL polarizations for (S) samples, which should relate to the generation of right-handed polarized states due to right-handed excitations. In addition, racemic samples show a slightly right-handed polarized state after right-handed excitations. These results show that the dominant polarization should originate from the intrinsic structure distortion of chiral perovskites rather than extrinsic injection of polarized photoexcitations. To understand the electron-phonon interaction in our chiral perovskites, we performed PL and CPL measurements on chiral perovskite samples at cryogenic temperatures (fig. S8). We find an increase in PL intensity and a large decrease of PL FWHM from ~150 meV at room temperature to ~28 meV at 4 K (fig. S8A), indicating a strong electron-
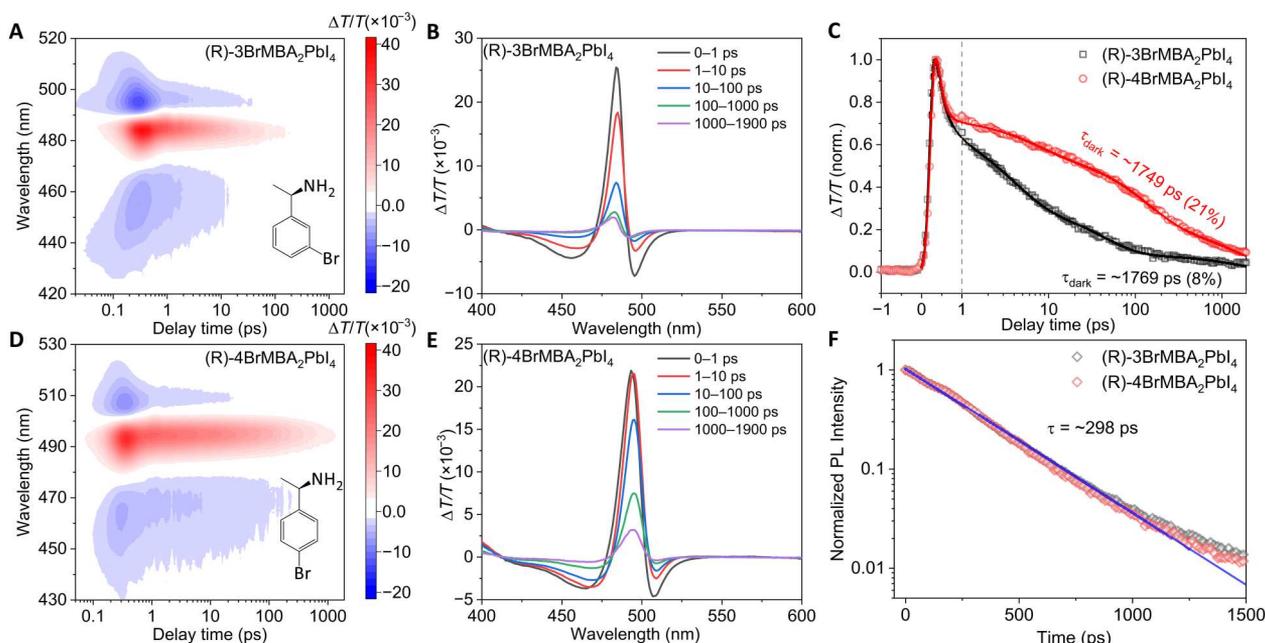
Fig. 3. Charge carrier dynamics of chiral perovskite thin films. (**A** and **D**) Linearly polarized TA maps, (**B** and **E**) time-resolved differential transmission spectra, (**C**) recombination kinetics collected at the GSB regions, and (**F**) TCSPC kinetics of (R)-3BrMBA$_2$PbI$_4$ and (R)-4BrMBA$_2$PbI$_4$ thin films, respectively. TA spectra were collected under 385-nm excitation with a pump fluence of ~1 μJ/cm^2, while TCSPC measurements were performed with photoexcitation at 405 nm and excitation fluence of ~10 μJ/cm^2.

phonon coupling in our chiral perovskites (16). Furthermore, there is another broad PL feature emerging at higher wavelength position, which we tentatively attribute to a trapped exciton. When we cooled down the chiral perovskite to 4 K, increased intensity differences between left-handed and right-handed PL detections were observed at free exciton position (P_{CPL} = ~60%; fig. S8B). On the basis of the results above, we conclude that our chiral 3BrMBA$_2$PbI$_4$ materials show PLQE and P_{CPL} values that are one order of magnitude larger than in previously reported chiral semiconductor materials (16, 42).

Characterization of excitation dynamics and radiative recombination

To resolve the mechanisms behind the bright PLQE and high degree of CPL of our chiral 2D perovskites, we investigated the excitation and relaxation dynamics via TA spectroscopy. TA color maps obtained from (R)-3BrMBA$_2$PbI$_4$ and (R)-4BrMBA$_2$PbI$_4$ spin-coated films (Fig. 3, A and D), using an excitation wavelength of 385 nm and fluence of ~1 μJ/cm^2, show ground state bleach (GSB) signals near the absorption edge, along with two photoinduced absorption (PIA) signals on either side of the GSB (43). The spectral and temporal evolutions of the TA spectra up to 2 ns are presented in Fig. 3 (B and E). We note that the TA signals of (R)-3BrMBA$_2$PbI$_4$ are blue-shifted compared to those of (R)-4BrMBA$_2$PbI$_4$. This effect is ascribed to a higher degree of structural distortion in (R)-3BrMBA cations (44), in agreement with the steady-state absorption and PL spectra (fig. S9). Furthermore, we note that the CD signals obtained from (R)-4BrMBA$_2$PbI$_4$ spin-coated films are smaller than (R)-3BrMBA$_2$PbI$_4$ samples (fig. S10). The grain sizes of (R)-3BrMBA$_2$PbI$_4$ and (R)-4BrMBA$_2$PbI$_4$ films are similar to each other (fig. S11), but (R)-3BrMBA$_2$PbI$_4$ films show more homogeneous surface structures and different crystallization orientations, which may also influence their chirality and optical features. We find that the TA decay in the GSB regions of (R)-3BrMBA$_2$PbI$_4$ is faster than that of (R)-4BrMBA$_2$PbI$_4$ (Fig. 3C). To quantify decay rates, a tetraexponential decay function was used (detailed fit results in table S4). We find that the main reason for the faster decay lifetime of (R)-3BrMBA$_2$PbI$_4$ is a suppressed population of a nonradiative decay channel. For both (R)-3BrMBA$_2$PbI$_4$ and (R)-4BrMBA$_2$PbI$_4$, the fitted nonradiative decay lifetime (τ_{dark}) is ~1700 ps, which suggests that some loss channels still remain, likely from defect states. However, the normalized amplitude of the nonradiative decay channel of (R)-3BrMBA$_2$PbI$_4$ is only ~8%, which is three times smaller than that of the reference material (R)-4BrMBA$_2$PbI$_4$ (~21%). We count this as the key mechanism underpinning the high PLQE value of (R)-3BrMBA$_2$PbI$_4$ samples. Fluence-dependent TA kinetics indicate that the nonradiative decay can be further reduced to ~6% with increased fluence (fig. S12A).

Figure 3F shows the time-correlated single-photon counting (TCSPC) kinetic plots of (R)-3BrMBA$_2$PbI$_4$ and (R)-4BrMBA$_2$PbI$_4$ thin films (excitation at 405 nm, ~10 μJ/cm^2). The PL decay kinetics for each sample are extracted at the excitonic PL peak position and are found to be nearly identical. For both materials, the PL kinetics fit well to a monoexponential decay with a fitted lifetime of ~300 ps. While this may be unexpected considering the higher PLQE for (R)-3BrMBA$_2$PbI$_4$, it is important to note that the PL decay only detects bright radiative recombination channels, while TA dynamics probe the kinetics of all photocarriers, including nonradiative decays (45) from dark or defect states in our 2D chiral perovskites. Thus, we attribute the observed differences in TA and PL kinetics to suppression of excitation transfer into dark states in (R)-3BrMBA$_2$PbI$_4$, which limits PLQEs in the reference (R)-4BrMBA$_2$PbI$_4$ materials. In addition, the absolute TCSPC intensity over the same acquisition times also indicates three times brighter emission in (R)-3BrMBA$_2$PbI$_4$ (fig. S13), which is consistent with the ratios of nonradiative decay that we observed from TA kinetics. Furthermore, TCSPC measurements show that the PL decay kinetics of chiral and racemic samples are similar (fig. S14).

Fluence-dependent TCSPC measurements (fig. S12B) indicate that the PL lifetime gradually decreases with increased fluence and then stabilizes beyond ~10 μJ/cm^2, which is consistent with our TA results. Generally, low fluence would result in more dominant effects from the population of dark states with slower decay rates, which increase the probability of nonradiative decay. Furthermore, such long-lived dark-state TA signals for both (R)-3BrMBA$_2$PbI$_4$ and (R)-4BrMBA$_2$PbI$_4$ persist for as long as a few microseconds, which we find in long-time TA spectroscopy (fig. S15). From the results above, we conclude that our cation engineering approach in chiral 3BrMBA$_2$PbI$_4$ reduces the population of dark states, which results in fast radiative emission that maintains circular polarization.

A tentative explanation for the reduction of nonradiative processes in (R)-3BrMBA$_2$PbI$_4$ compared to (R)-4BrMBA$_2$PbI$_4$ can be proposed on the basis of inspection of the structural distortions in the crystallographic structures of (S)-3BrMBA$_2$PbI$_4$ and (S)-4BrMBA$_2$PbI$_4$. The β angle disparity $\Delta\beta = \beta_{max} - \beta_{min}$ is larger in (S)-3BrMBA$_2$PbI$_4$ ($\Delta\beta$ = 11.9°) than in (S)-4BrMBA$_2$PbI$_4$ ($\Delta\beta$ = 8.9°), which is a necessary condition to obtain a larger polar distortion and, in turn, a larger Rashba effect (vide infra) (35), and further explains the higher degree of CPL that we obtained in chiral 3BrMBA$_2$PbI$_4$. However, the β angle is homogeneously distributed in the crystallographic structure of (S)-3BrMBA$_2$PbI$_4$, taking only two distinct values (β_{min} = 141.3° and β_{max} = 153.2°). By comparison, the β angle takes six different values in the crystallographic structure of (S)-4BrMBA$_2$PbI$_4$, spread between 148.2° and 157.5° and is changing from one perovskite layer to the other. These structural differences suggest that larger microstrain effects might be the origin of enhanced nonradiative processes in chiral 4BrMBA$_2$PbI$_4$.

Time-resolved spin-polarization results

To investigate the origin of the remarkably high degree of CPL at room temperature, we performed CTA spectroscopy. For this, we controlled the circular polarizations of pump and probe beams with linear polarizers and quarter waveplates. CTA spectra collected from (R)-3BrMBA$_2$PbI$_4$, for all four polarized pump-probe configurations, at indicated delay times, are shown in Fig. 4A. The evolution of the CTA spectra up to 7200 ps is presented in fig. S16 (A to E). Following excitation with σ$^+$ or σ$^-$ photons at 385 nm (fluence, ~2.5 μJ/cm^2), a clear intensity difference is observed when probing (R)-3BrMBA$_2$PbI$_4$ with σ$^+$ and σ$^-$ photons. This difference is most pronounced in the PIA regions, at all delay times, which confirms the persistence of long-lived polarized photoexcitations. Thus, we extracted the decay and polarization kinetics at the PIA spectral regions (gray regions in Fig. 4A). Compared to the counterpolarized pump-probe configuration, the TA signals with copolarized configurations always show higher intensities (Fig. 4B), as expected (46, 47). However, in nonchiral systems measured in copolarized TA configurations, signals from co- and counterpolarized pump-
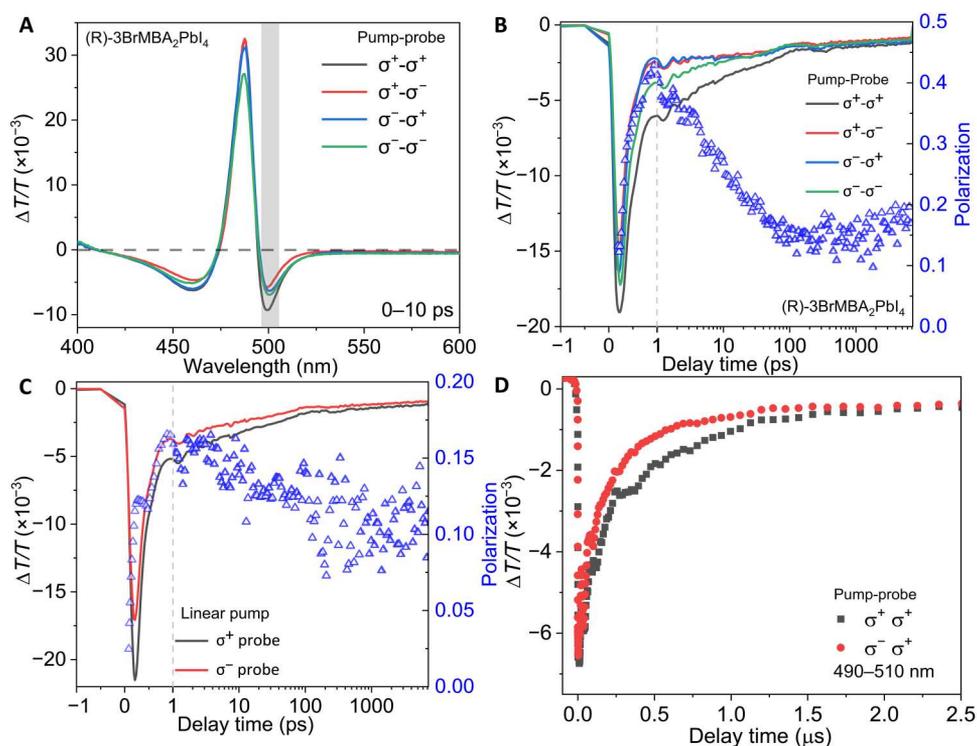
Fig. 4. CTA spectroscopy of chiral (R)-3BrMBA$_2$PbI$_4$ perovskites, under 385-nm excitation with a pump fluence of ~2.5 μJ/cm^2 (nanosecond regime) and ~50 μJ/cm^2 (microsecond regime). (**A** and **B**) CTA spectra and kinetics showing the difference between four circularly polarized configurations. The different polarizations of pump and probe pulses are indicated σ$^+$ (right-handed) or σ$^-$ (left-handed). The spectra shown in (A) are averaged over the initial 10 ps. Decay kinetics are extracted over the gray spectral range in (A), and the polarization relaxation kinetics between black and red curves are calculated and plotted as blue triangles. (**C**) Comparison of TA kinetics with linear pump and circularly polarized probes showing net circular polarization. (**D**) Long-term CTA kinetics obtained from the PIA region between 490 and 510 nm. At room temperature, chiral (R)-3BrMBA$_2$PbI$_4$ shows different depolarization kinetics for σ$^+$ and σ$^-$ states, even under linear polarization of optical excitation.

probe display the same depolarization kinetics (*43*). Unexpectedly, for our chiral (R)-3BrMBA$_2$PbI$_4$, signals from co- and counterpolarized pump-probe configurations show different depolarization kinetics and TA signals, with σ$^+$-σ$^+$ pump-probe exhibiting higher intensities.

We find that the signals for copolarized configurations show higher initial TA intensities around time zero, as well as slower recombination rates during the first picoseconds, than signals for counterpolarized configurations (fig. S17A), i.e., the net polarization of the excitation population increases. This can be understood by considering that, in addition to the polarized states generated from circularly polarized photoexcitations, the chirality of the perovskite would initially produce more strongly polarized states, according to D'yakonov-Perel mechanisms (*48*) due to the highly distorted structures with broken inversion symmetry. To quantify these effects, we thus calculate the associated degree of polarization (P_{CTA}) and plot the depolarization kinetics as blue triangles in Fig. 4B. In particular, the degrees of CTA polarization were determined by the following equation

$$P_{CTA} = \frac{\Delta T/T_{counter} - \Delta T/T_{co}}{\Delta T/T_{counter} + \Delta T/T_{co}}$$

where $\Delta T/T_{counter}$ and $\Delta T/T_{co}$ are the TA signals with counter- and copolarized configurations, respectively. Around time zero, the degree of polarization of (R)-3BrMBA$_2$PbI$_4$ shows a positive signal, starting from a level of ~10% and gradually increases over

the first picoseconds to 45%. The degree of polarization then decays over the next 100 ps and finally stabilizes at ~20% until the end of our detection range (7200 ps).

To further investigate the polarization dynamics of the photoexcitations, we applied a linearly polarized pump to excite the chiral perovskites and then detected the TA signals with circularly polarized probes. As shown in Fig. 4C, the chiral (R)-3BrMBA$_2$PbI$_4$ materials exhibit different decay kinetics for σ$^+$ and σ$^-$ probes. The degree of polarization for σ$^+$ and σ$^-$ probe starts from 0% at time zero and increases to the maximum positive value of ~17% during the initial 1 ps, after which it decays to ~10% at 7200 ps. This increase in the polarization after time zero indicates that in chiral (R)-3BrMBA$_2$PbI$_4$, the decay of excited states with σ$^+$ symmetry is slower than that for σ$^-$ symmetry (fig. S17B). Consistent with the CPL results, opposite chirality features of (R)- and (S)-3BrMBA$_2$PbI$_4$ result in reversed signals in linear pump-σ$^+$ and pump-σ$^-$ probe TA kinetics. Furthermore, we also performed CTA spectroscopy measurements on chiral (S)-3BrMBA$_2$PbI$_4$ samples with linear pump and circularly polarized probes, which confirm that the dominant population of photoexcited states in chiral (S)-3BrMBA$_2$PbI$_4$ show negative values for the degree of CTA polarization (fig. S19).

We note that the highest degree of TA polarization under linear excitation is smaller than the degree of CPL (~52%). This apparent difference arises because PL only detects the bright states, while TA collects the signals from all states, including both bright and dark

states, as discussed above. Combining the measured CPL degree of ~52% and the PLQE value of 39% of our chiral perovskites, the estimated degree of polarization of all states is ~20% (PLQE × CPL degree), which is in agreement with the degree of TA polarization that we measured (Fig. 4C). We take this as an indication that the polarized states of chiral perovskites are predominantly derived from bright states.

As the degrees of polarization for chiral perovskites (R)-3BrMBA$_2$PbI$_4$ samples do not converge to zero at the limit of our short-term TA measurements (7200 ps), we further used CTA measurements up to microsecond time delays on chiral (R)-3BrMBA$_2$PbI$_4$ and plotted their kinetics in Fig. 4D (corresponding spectra in fig. S16F). Under circularly polarized excitation at 385 nm, the difference between co- and counterpolarized TA signals persists for as long as 2 μs. This microsecond polarization lifetime in our materials is, to the best of our knowledge, the longest value observed in lead-halide perovskite systems (46, 49). Together, the intrinsic polarized states associated with the distorted crystal structures and the long-lived chirality-dependent polarized excitons in chiral perovskites, which persist even longer than their fast PL decay lifetime (Fig. 3F), explain the high and efficient CPL results at room temperature.

## Electronic structure results from first-principles calculations

Additional insight is provided by investigation of the electronic structure of Rac- and (S)-3BrMBA$_2$PbI$_4$ by means of density functional theory (DFT)–based calculations. The band structure of the racemic compound (Fig. 5A and fig. S20) shows a direct bandgap at the Y point in the Brillouin zone, as well as the well-known characteristics of layered metal-halide perovskites, i.e., large dispersion in the perovskite plane and flat bands along the stacking axis (bandwidth smaller than 1 meV) (50, 51). The valence band maximum (VBM) is composed primarily of iodine 5p orbitals with lead 6s contributions, while the conduction band minimum (CBM) is dominated by lead 6p orbitals with small contributions from iodine 5p (Fig. 5B and fig. S21).

When moving to (S)-3BrMBA$_2$PbI$_4$, the main features of the band structure are preserved (Fig. 5C and fig. S22). However,

important differences can also be observed, such as the opening of the bandgap by 80 meV as a result of larger structural distortion (vide supra), which is consistent with the experimentally observed blue shift in absorption and PL spectra. The band structure of (S)-3BrMBA$_2$PbI$_4$ (Fig. 5C and fig. S22) reveals the splitting of the conduction bands induced by the Rashba coupling, which arises from the loss of centrosymmetry and the large SOC in lead- and iodine-based compounds (52). However, because the polar axis of the structure is perpendicular to the stacking axis, the coupling is incomplete and the splitting can be observed only in one direction (B-A), while it is dispersionless in the other direction (B-Γ; figs. S22 and S23) (53). This results in a special spin texture, where the spin orientation remains constant in each half-plane of the Brillouin zone (Fig. 5D). We also note that, because of the presence of the in-plane polar axis in the crystallographic structure of (S)-3BrMBA$_2$PbI$_4$, the spin degeneracy is recovered along the B-D line. Therefore, a perfect CD resulting from isotropic in-plane spin-splitting is not expected and might be at the origin of a maximum CPL below 100%.

In the valence band, the effect is weak with a shift of the VBM in k-space, k_R, smaller than 0.01 Å^{-1} and an energy splitting of 0.50 meV, leading to the Rashba parameter $\alpha_{VBM} = 0.08$ eV·Å (see fig. S23 for notations). The effect is much larger in the conduction band, with a large displacement of the CBM away from the B point (0.02 Å^{-1}) and a 75-meV splitting, thus yielding a large Rashba parameter of $\alpha_{CBM} = 2.21$ eV·Å, which compares well with previously computed parameters in lead-iodide perovskites (14). This much larger Rashba effect in the conduction band, compared to valence band, may also explain the larger difference between their g_{lum} and g_{abs} values. We note that such a large computed Rashba parameter is consistent with the strong β angle disparity in the structure of (S)-3BrMBA$_2$PbI$_4$ (Δβ = 11.9°), which falls in the category of compounds with Δβ > 11° exhibiting sizeable spin-splitting (35).

Last, we compare the electronic structures of Rac- and (S)-3BrMBA$_2$PbI$_4$ with the ones of the Rac- and (S)-4BrMBA$_2$PbI$_4$ compounds (fig. S24). The band structures of the 4BrMBA-based perovskites present the same features, with a direct bandgap for the racemic compound that becomes slightly indirect for the (S)
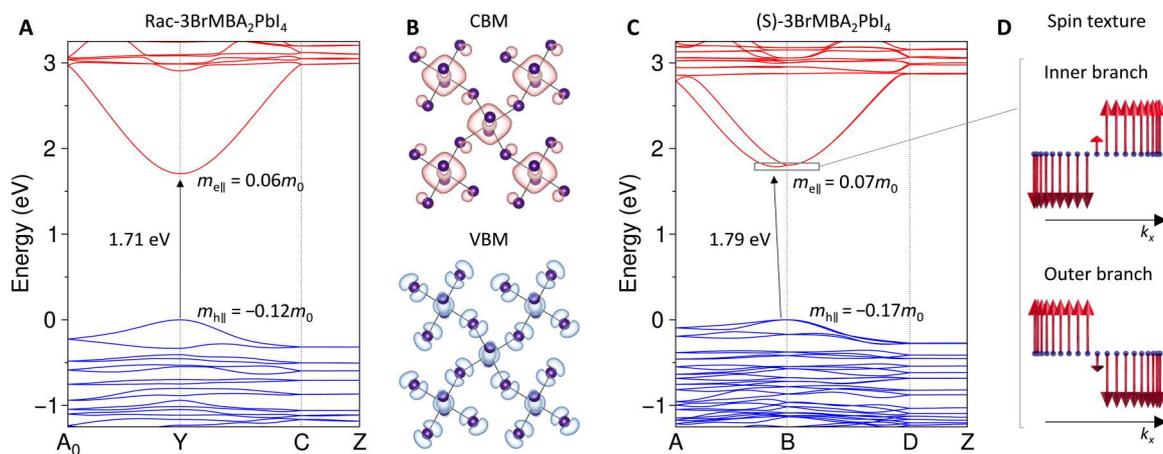
Fig. 5. Electronic structure of layered (Rac/S)-3BrMBA$_2$PbI$_4$ perovskites. (**A** and **C**) DFT computed band structures of Rac-3BrMBA$_2$PbI$_4$ and (S)-3BrMBA$_2$PbI$_4$, respectively. In-plane hole ($m_{h\parallel}$) and electron ($m_{e\parallel}$) effective masses are computed at the valence and conduction band edges. (**B**) Partial charge density taken at the VBM and CBM. (**D**) Spin textures computed for the (S) structure in the (k_x, k_y) plane for the inner and outer branches of the conduction bands.

structure because of the same incomplete Rashba splitting observed in the CBM and VBM. With respect to (S)-3BrMBA$_2$PbI$_4$, the coupling is one order of magnitude stronger in the valence bands but remains small with α_{VBM} = 0.82 eV·Å and much smaller at the conduction bands with α_{CBM} = 0.64 eV·Å. As mentioned above, (S)-4BrMBA$_2$PbI$_4$ exhibits a smaller β angle disparity ($\Delta\beta$ = 8.9°) than (S)-3BrMBA$_2$PbI$_4$, leading, in principle, to a less favorable situation for spin-based properties. Moreover, the enhanced microstrain in the structure may trigger larger nonradiative processes. Compared to the reference samples (R)-4BrMBA$_2$PbI$_4$, the exciton peak position of the chiral (R)-3BrMBA$_2$PbI$_4$ samples shows a small shift (~40 meV) in absorption spectra (fig. S9). The calculated bandgap of (R)-3BrMBA$_2$PbI$_4$ is larger than for (R)-4BrMBA$_2$PbI$_4$ (~120 meV; fig S24), thus indicating the increase of net exciton binding energy by ~80 meV. With the reported binding energy of (R)-4BrMBA$_2$PbI$_4$ being ~170 meV (16), we conclude that the observed variation of exciton binding energies will only have a very small effect on their recombination dynamics (54).

To elucidate the origin of our high PLQE and degree of CPL values of chiral (R)-3BrMBA$_2$PbI$_4$ samples, we used identical fabrication methods to prepare related chiral 2D perovskite single crystals and thin films for comparison, such as the highly reported (R)-MBA$_2$PbI$_4$, i.e., without the Br functional group, (R)-4BrMBA$_2$PbI$_4$ and (R)-2BrMBAPbI$_3$ with the Br in para or ortho position, and (R)-3ClMBA$_2$PbI$_4$ with Cl to compare for changes in halide type and position on the aromatic rings. None of these show comparable performance features as chiral (R)-3BrMBA$_2$PbI$_4$ samples with both high PLQE and large degree of CPL (see detailed comparisons in the Supplementary Materials). Thus, we conclude that, specifically, the chiral 3BrMBA molecules form a particularly suitable perovskite crystal structure for bright emission and strongly polarized CPL.

Considering their promising chiral optical features, we also fabricated circularly polarized photodetectors and PeLEDs based on our chiral layered perovskites. The average $g_{current}$ of our chiral circularly polarized photodetector is ~0.5% under 490-nm excitations (fig. S30), which is slightly larger than expected from our CD results, likely because of additional effects from spin-related carrier generation and transport (26, 55). For circularly polarized LEDs, because of their low conductivity and stability, LEDs using pure 2D perovskite (N = 1) emitters experience electrical breakdown before turning on, which is also a general problem for other pure 2D phase PeLEDs (15). We then mixed the 2D phase with 3D phase to get quasi-2D chiral perovskites for efficient emitting layer (fig. S31). We found that N = 2 phase shows a weak electroluminescence, which provides a proof of concept that our chiral perovskite materials are capable of application in optoelectronic devices. However, the device shows insufficient performance to detect reliable circularly polarized electroluminescence. We expect that the addition of doping atoms, changing the ratios between mixed 2D/3D phases, or nanocrystal-in-bulk heterostructures can improve device performance. Thus, from our study, we find that chiral 3BrMBA molecules provide an excellent option to increase the perovskite crystal angle distortion degrees, resulting in outstanding chiral optical features, as well as structure configurations that strongly decrease the impact of nonradiative loss channels during recombination, resulting in fast radiative decay with large PLQE value.

In summary, we report that chiral 2D HMHPs

(R/S)-3BrMBA$_2$PbI$_4$, show large PLQE values and a high degree of CPL. By engineering the position of Br atom on the aromatic ring from para- to metaposition, we find that chiral 3BrMBA$_2$PbI$_4$ samples have crystal structures with a higher degree of distortion and show improved chiroptical properties, compared to chiral 4BrMBA$_2$PbI$_4$. Because of their more distorted crystal structures, chiral 3BrMBA$_2$PbI$_4$ perovskites exhibit a highly improved CPL degree up to 52% under linear excitation at room temperature. PLQE measurements reveal that chiral 3BrMBA$_2$PbI$_4$ has a dominantly radiative decay channel with a quantum efficiency of 39%. Such high CPL degree and large PLQE value exceeds most reported chirality-related materials, including traditional spintronic materials, such as GaAs or chiral organic semiconductors (table S1). Our experimental and theoretical findings on chiral layered HMHPs with bright and strong CPL highlights the unexpected ability of the hybrid perovskites to balance strong chirality with excellent optoelectronic properties. We expect our materials to show potential as light emitters in circularly polarized LEDs and spintronic applications at room temperature.

MATERIALS AND METHODS
Synthesis of layered (R/S/racemic)-3BrMBA$_2$PbI$_4$ single crystals and thin films
Chemicals, such as PbI$_2$, HI, DMF, racemic, and (S)-3BrMBA, were purchased from Sigma-Aldrich, and (R)-3BrMBA was ordered from Alfa Aesar. All chemicals were used without further purification. As a general synthesis procedure of layered perovskite single crystals, 0.231 g of PbI$_2$ and 151 µl of (R), (S), or racemic-3BrMBA were separately dissolved in 6 ml of HI by heating at 90°C for 30 min. After adding 1 ml of H$_2$O into the solution, the mixture was further transferred into a 25-ml autoclave and allowed to react at 95°C for 24 hours. On cooling the solution slowly to room temperature with a cooling rate of 0.5°C/hour, orange plate–like single crystals formed gradually. In contrast, a relatively fast cooling rate resulted in needle-like single crystals or powder samples. The perovskite thin-film fabrication was performed in a nitrogen-filled glove box using glass coverslips that had been previously treated with oxygen plasma for 5 min as substrates. First, 40 mg of as-synthesized perovskite crystals or powders were dissolved in 200 µl of DMF to prepare precursor solutions. After that, the precursor solution was spin-coated on the glass substrates with a rotation speed of 4000 rpm for 35 s, after which they were annealed at 90°C for 10 min. The obtained perovskite thin films were stored inside the glove box for further characterization.

XRD measurements
SCXRD data were obtained at 100 K on a Bruker D8 Venture system with a Helios optic monochromator and Mo radiation (λ = 0.71073 Å). The detailed data collection and refinement information are further summarized in table S2 and the corresponding cif. documents. XRD patterns of thin films were collected by an x-ray diffractometer (Rigaku SmartLab) with Cu Kα irradiation.

DFT calculations
First-principles calculations were carried out on the basis of DFT, as implemented in the SIESTA package (56, 57). The nonlocal van der Waals density functional of Dion et al. (58) corrected by Cooper (C09) was used for geometry optimizations of the organic cations

(59). SOC was taken into account through the so-called off-site approach as following the Hemstreet formalism (60). Core electrons were described with Troullier-Martins pseudopotentials (61), while valence wave functions were developed over double-ζ polarized basis set of finite-range numerical pseudoatomic orbitals (62). In all cases, an energy cutoff of 150 rydberg for real-space mesh size was used, and the Brillouin zone was sampled using a $8 \times 8 \times 2$ grid. Experimental structures of (S/racemic)-3BrMBA$_2$PbI$_4$ were used for the inorganic skeleton, well characterized by XRD, while the positions of organic cations were optimized.

General optical measurements

The CD and absorption spectroscopy data were collected by a CD spectrometer (JASCO J-815). PL measurements were carried out using a setup with a 405-nm excitation laser (PicoQuant PDL 800-D) and a Horiba iHR 550 spectrometer. A single-photon avalanche photodiode detector (Micro Photon Devices PD-100-CTE) and a constant fraction discriminator (PicoQuant PicoHarp 300) were further used for TCSPC measurements.

PLQE measurements

PLQE measurements were performed using the method proposed by de Mello et al. (63). Briefly, perovskite samples were excited with a 405-nm continuous wave laser, while the PL value was collected by an Andor Shamrock spectrometer and Andor iDus CCD array. The signals were recorded from an integrating sphere in three different configurations, without sample, with laser on the sample, and with laser off the sample, respectively. Each measurement was further performed three times to get comparable average results.

CPL measurements

CPL measurements were performed on single-crystal samples, with a 405-nm linear excitation, which is provided by a Yb:yttrium-aluminum-garnet laser system (Light Conversion Pharos) with an optical parametric amplifier (Light Conversion Orpheus). Then, the green emission was collected by a 50× long working distance objective (Mitutoyo) and passed through a quarter waveplate to transfer the CPL signals to linearly polarized signals. After that, a Wollaston prism followed by a 45° linear polarizer was used to spatially separate the right-handed and left-handed polarized PL. Both right-handed and left-handed polarized PL were collected on two regions of interest on the ICCD camera (Andor, iStar) at the same time to get rid of the influence from sample degradation or from excitations. Both MAPbBr$_3$ and Rac-3BrMBA$_2$PbI$_4$ were used as reference samples.

TA spectroscopy

Three pump-probe setups were used for TA measurements. For short-time TA measurements (1900 ps), A 270-fs pulsed laser (5-kHz repetition rate, 770 nm) was first generated from the same laser system that we used for CPL measurements. The generated laser was further split into pump and probe beam paths. The pump beam (385 nm) was obtained by focusing the original laser (770 nm) through a beta barium borate crystal, and the probe beam was a white light continuum, which was produced by pumping the original laser into a CaF$_2$ window. A linear translation stage (Newport DLS325) was used to provide the delay stages between pump and probe beams. A spectrometer (Andor Kymera 193i) and a scientific complementary metal-oxide semiconductor camera (Andor Zyla 5.5) were further used to collect the transmitted probe spectrum for every pulse. Linear polarizers and quarter waveplates were applied to control the polarization directions of pump and probe beams for CTA measurements. For TA measurements with 7700 ps and microsecond time scales, commercial TA spectrometers were used (Ultrafast Systems, HELIOS and EOS).

Supplementary Materials

This PDF file includes:
Comparison of different chiral 2D perovskites
Tables S1 to S4
Figs. S1 to S31

Other Supplementary Material for this manuscript includes the following:
Data S1 and S2

REFERENCES AND NOTES

1. R. Naaman, D. H. Waldeck, Chiral-induced spin selectivity effect. *J. Phys. Chem. Lett.* **3**, 2178–2187 (2012).

2. B. Göhler, V. Hamelbeck, T. Z. Markus, M. Kettner, G. F. Hanne, Z. Vager, R. Naaman, H. S. Zacharias, Spin selectivity in electron transmission through self-assembled monolayers of double-stranded DNA. *Science* **331**, 894–897 (2011).

3. Y. Yang, R. C. da Costa, D. M. Smilgies, A. J. Campbell, M. J. Fuchter, Induction of circularly polarized electroluminescence from an achiral light-emitting polymer via a chiral small-molecule dopant. *Adv. Mater.* **25**, 2624–2628 (2013).

4. N. Nishizawa, K. Nishibayashi, H. Munekata, Pure circular polarization electroluminescence at room temperature with spin-polarized light-emitting diodes. *Proc. Natl. Acad. Sci. U.S.A* **114**, 1783–1788 (2017).

5. Y.-H. Kim, Y. Zhai, H. Lu, X. Pan, C. Xiao, E. A. Gaulding, S. P. Harvey, J. J. Berry, Z. Valy Vardeny, J. M. Luther, M. C. Beard, Chiral-induced spin selectivity enables a room-temperature spin light-emitting diode. *Science* **371**, 1129–1133 (2021).

6. H. Shigemitsu, K. Kawakami, Y. Nagata, R. Kajiwara, S. Yamada, T. Mori, T. Kida, Cyclodextrins with multiple pyrenyl groups: An approach to organic molecules exhibiting bright excimer circularly polarized luminescence. *Angew. Chem. Int. Ed.* **61**, e202114700 (2022).

7. X. Jiang, X. Liu, Y. Jiang, Y. Quan, Y. Cheng, C. Zhu, Fluorescence study of chiral β-ketoiminate-based newly synthesized boron hybrid polymers. *Macromol. Chem. Phys.* **215**, 358–364 (2014).

8. H. Wu, X. He, B. Yang, C. C. Li, L. Zhao, Assembly-induced strong circularly polarized luminescence of spirocyclic chiral silver(I) clusters. *Angew. Chem. Int. Ed.* **60**, 1535–1539 (2021).

9. J. Hao, Y. Li, J. Miao, R. Liu, J. Li, H. Liu, Q. Wang, H. Liu, M. H. Delville, T. He, K. Wang, X. Zhu, J. Cheng, Ligand-induced chirality in asymmetric CdSe/CdS nanostructures: A close look at chiral tadpoles. *ACS Nano* **14**, 10346–10358 (2020).

10. G. Sallen, S. Kunz, T. Amand, L. Bouet, T. Kuroda, T. Mano, D. Paget, O. Krebs, X. Marie, K. Sakoda, B. Urbaszek, Nuclear magnetization in gallium arsenide quantum dots at zero magnetic field. *Nat. Commun.* **5**, 3268 (2014).

11. T. Wu, Y. Wang, Z. Dai, D. Cui, T. Wang, X. Meng, E. Bi, X. Yang, L. Han, Efficient and stable CsPbI$_3$ solar cells via regulating lattice distortion with surface organic terminal groups. *Adv. Mater.* **31**, e1900605 (2019).

12. H. Lei, D. Hardy, F. Gao, Lead-free double perovskite Cs$_2$AgBiBr$_6$: Fundamentals, applications, and perspectives. *Adv. Funct. Mater.* **31**, 2105898 (2021).

13. Q. Wei, Z. Ning, Chiral perovskite spin-optoelectronics and spintronics: Toward judicious design and application. *ACS Mater. Lett.* **3**, 1266–1275 (2021).

14. M. Kepenekian, J. Even, Rashba and Dresselhaus couplings in halide perovskites: Accomplishments and opportunities for spintronics and spin-orbitronics. *J. Phys. Chem. Lett.* **8**, 3362–3370 (2017).

15. G. Grancini, M. K. Nazeeruddin, Dimensional tailoring of hybrid perovskites for photovoltaics. *Nat. Rev. Mater.* **4**, 4–22 (2019).

16. Y. Qin, F. F. Gao, S. Qian, T. M. Guo, Y. J. Gong, Z. G. Li, G. D. Su, Y. Gao, W. Li, C. Jiang, P. Lu, X. H. Bu, Multifunctional chiral 2D lead halide perovskites with circularly polarized photoluminescence and piezoelectric energy harvesting properties. *ACS Nano* **16**, 3221–3230 (2022).

17. Y. Hu, F. Florio, Z. Chen, W. Adam Phelan, M. A. Siegler, Z. Zhou, Y. Guo, R. Hawks, J. Jiang, J. Feng, L. Zhang, B. Wang, Y. Wang, D. Gall, E. F. Palermo, Z. Lu, X. Sun, T.-M. Lu, H. Zhou,

Y. Ren, E. Wertz, R. Sundararaman, J. Shi, A chiral switchable photovoltaic ferroelectric 1D perovskite. *Sci. Adv.* **6**, eaay4213 (2020).

18. M. Wang, H. Xu, T. Wu, H. Ambaye, J. Qin, J. Keum, I. N. Ivanov, V. Lauter, B. Hu, Optically induced static magnetization in metal halide perovskite for spin-related optoelectronics. *Adv. Sci.* **8**, 2004488 (2021).

19. J. Ahn, E. Lee, J. Tan, W. Yang, B. Kim, J. Moon, A new class of chiral semiconductors: Chiral-organic-molecule-incorporating organic-inorganic hybrid perovskites. *Mater. Horiz.* **4**, 851–856 (2017).

20. G. Long, C. Jiang, R. Sabatini, Z. Yang, M. Wei, L. N. Quan, Q. Liang, A. Rasmita, M. Askerka, G. Walters, X. Gong, J. Xing, X. Wen, R. Quintero-Bermudez, H. Yuan, G. Xing, X. R. Wang, D. Song, O. Voznyy, M. Zhang, S. Hoogland, W. Gao, Q. Xiong, E. H. Sargent, Spin control in reduced-dimensional chiral perovskites. *Nat. Photonics* **12**, 528–533 (2018).

21. H. Lu, J. Wang, C. Xiao, X. Pan, X. Chen, R. Brunecky, J. J. Berry, K. Zhu, M. C. Beard, Z. Valy Vardeny, Spin-dependent charge transport through 2D chiral hybrid lead-iodide perovskites. *Sci. Adv.* **5**, eaay0571 (2019).

22. M. W. Heindl, T. Kodalle, N. Fehn, L. K. Reb, S. Liu, C. Harder, M. Abdelsamie, L. Eyre, I. D. Sharp, S. V. Roth, P. Müller-Buschbaum, A. Kartouzian, C. M. Sutter-Fella, F. Deschler, Strong induced circular dichroism in a hybrid lead-halide semiconductor using chiral amino acids for crystallite surface functionalization. *Adv. Opt. Mater.* **10**, 2200204 (2022).

23. S. Liu, M. W. Heindl, N. Fehn, S. Caicedo-Dávila, L. Eyre, S. M. Kronawitter, J. Zerhoch, S. Bodnar, A. Shcherbakov, A. Stadlbauer, G. Kieslich, I. D. Sharp, D. A. Egger, A. Kartouzian, F. Deschler, Optically induced long-lived chirality memory in the color-tunable chiral lead-free semiconductor (R)/(S)-CHEA₄Bi₂Br$_x$I₁₀₋$_x$ (x= 0−10). *J. Am. Chem. Soc.* **144**, 14079–14089 (2022).

24. M. K. Jana, R. Song, H. Liu, D. R. Khanal, S. M. Janke, R. Zhao, C. Liu, Z. Valy Vardeny, V. Blum, D. B. Mitzi, Organic-to-inorganic structural chirality transfer in a 2D hybrid perovskite and impact on Rashba-Dresselhaus spin-orbit coupling. *Nat. Commun.* **11**, 4699 (2020).

25. J. Ma, C. Fang, C. Chen, L. Jin, J. Wang, S. Wang, J. Tang, D. Li, Chiral 2D perovskites with a high degree of circularly polarized photoluminescence. *ACS Nano* **13**, 3659–3665 (2019).

26. G. Long, R. Sabatini, M. I. Saidaminov, G. Lakhwani, A. Rasmita, X. Liu, E. H. Sargent, W. Gao, Chiral-perovskite optoelectronics. *Nat. Rev. Mater.* **5**, 423–439 (2020).

27. T. Liu, W. Shi, W. Tang, Z. Liu, B. C. Schroeder, O. Fenwick, M. J. Fuchter, High responsivity circular polarized light detectors based on quasi two-dimensional chiral perovskite films. *ACS Nano* **16**, 2682–2689 (2022).

28. J. Wang, C. Fang, J. Ma, S. Wang, L. Jin, W. Li, D. Li, Aqueous synthesis of low-dimensional lead halide perovskites for room-temperature circularly polarized light emission and detection. *ACS Nano* **13**, 9473–9481 (2019).

29. F. F. Gao, X. Li, Y. Qin, Z. G. Li, T. M. Guo, Z. Z. Zhang, G. D. Su, C. Jiang, M. Azeem, W. Li, X. Wu, X. H. Bu, Dual-stimuli-responsive photoluminescence of enantiomeric two-dimensional lead halide perovskites. *Adv. Opt. Mater.* **9**, 2100003 (2021).

30. D. di Nuzzo, L. Cui, J. L. Greenfield, B. Zhao, R. H. Friend, S. C. J. Meskers, Circularly polarized photoluminescence from chiral perovskite thin films at room temperature. *ACS Nano* **14**, 7610–7616 (2020).

31. L. Yao, G. Niu, J. Li, L. Gao, X. Luo, B. Xia, Y. Liu, P. Du, D. Li, C. Chen, Y. Zheng, Z. Xiao, J. Tang, Circularly polarized luminescence from chiral tetranuclear copper(I) iodide clusters. *J. Phys. Chem. Lett.* **11**, 1255–1260 (2020).

32. J. X. Gao, W. Y. Zhang, Z. G. Wu, Y. X. Zheng, D. W. Fu, Enantiomorphic perovskite ferro-electrics with circularly polarized luminescence. *J. Am. Chem. Soc.* **142**, 4756–4761 (2020).

33. X. Yang, M. Zhou, Y. Wang, P. Duan, Electric-field-regulated energy transfer in chiral liquid crystals for enhancing upconverted circularly polarized luminescence through steering the photonic bandgap. *Adv. Mater.* **32**, 2000820 (2020).

34. H. Lu, C. Xiao, R. Song, T. Li, A. E. Maughan, A. Levin, R. Brunecky, J. J. Berry, D. B. Mitzi, V. Blum, M. C. Beard, Highly distorted chiral two-dimensional tin iodide perovskites for spin polarized charge transport. *J. Am. Chem. Soc.* **142**, 13030–13040 (2020).

35. M. K. Jana, R. Song, Y. Xie, R. Zhao, P. C. Sercel, V. Blum, D. B. Mitzi, Structural descriptor for enhanced spin-splitting in 2D hybrid perovskites. *Nat. Commun.* **12**, 4982 (2021).

36. F. E. Neumann, O. E. Meyer, *Vorlesungen über die Theorie der Elasticität der festen Körper und des Lichtäthers, gehalten an der Universität Königsberg* (BG Teubner, 1885), vol. 4.

37. P. Curie, Sur la symétrie dans les phénomènes physiques, symétrie d'un champ électrique et d'un champ magnétique. *J. Phys. Theor. Appl.* **3**, 393–415 (1894).

38. S. Gull, M. H. Jamil, X. Zhang, H.-S. Kwok, G. Li, Stokes shift in inorganic lead pe-rovskites: Current status and perspective. *ChemistryOpen* **11**, e2021002 (2022).

39. Y. Shi, P. Duan, S. Huo, Y. Li, M. Liu, Endowing perovskite nanocrystals with circularly po-larized luminescence. *Adv. Mater.* **30**, 1705011 (2018).

40. Z. Wen, R. Lu, F. Gu, K. Zheng, L. Zhang, H. Jin, Y. Chen, S. Wang, S. Pan, Enabling efficient blue-emissive circularly polarized luminescence by in situ crafting of chiral quasi-2D pe-rovskite nanosheets within polymer nanofibers. *Adv. Funct. Mater.* **33**, 2212095 (2023).

41. T. Neumann, S. Feldmann, P. Moser, A. Delhomme, J. Zerhoch, T. van de Goor, S. Wang, M. Dyksik, T. Winkler, J. J. Finley, P. Plochocka, M. S. Brandt, C. Faugeras, A. V. Stier,

F. Deschler, Manganese doping for enhanced magnetic brightening and circular polari-zation control of dark excitons in paramagnetic layered hybrid metal-halide perovskites. *Nat. Commun.* **12**, 3489 (2021).

42. J. T. Lin, D. G. Chen, L. S. Yang, T. C. Lin, Y. H. Liu, Y. C. Chao, P. T. Chou, C. W. Chiu, Tuning the circular dichroism and circular polarized luminescence intensities of chiral 2D hybrid organic–inorganic perovskites through halogenation of the organic ions. *Angew. Chem. Int. Ed.* **60**, 21434–21440 (2021).

43. S. A. Bourelle, R. Shivanna, F. V. A. Camargo, S. Ghosh, A. J. Gillett, S. P. Senanayak, S. Feldmann, L. Eyre, A. Ashoka, T. W. J. van de Goor, H. Abolins, T. Winkler, G. Cerullo, R. H. Friend, F. Deschler, How exciton interactions control spin-depolarization in layered hybrid perovskites. *Nano Lett.* **20**, 5678–5685 (2020).

44. K. Z. Du, Q. Tu, X. Zhang, Q. Han, J. Liu, S. Zauscher, D. B. Mitzi, Two-dimensional lead(II) halide-based hybrid perovskites templated by acene alkylamines: Crystal structures, optical Properties, and piezoelectricity. *Inorg. Chem.* **56**, 9291–9302 (2017).

45. R. L. Z. Hoye, L. Eyre, F. Wei, F. Brivio, A. Sadhanala, S. Sun, W. Li, K. H. L. Zhang, J. L. MacManus-Driscoll, P. D. Bristowe, R. H. Friend, A. K. Cheetham, F. Deschler, Funda-mental carrier lifetime exceeding 1 μs in Cs₂AgBiBr₆ double perovskite. *Adv. Mater. Inter-faces* **5**, 1800464 (2018).

46. W. Liang, Y. Li, D. Xiang, Y. Han, Q. Jiang, W. Zhang, K. Wu, Efficient optical orientation and slow spin relaxation in lead-free CsSnBr₃ perovskite nanocrystals. *ACS Energy Lett.* **6**, 1670–1676 (2021).

47. W. Zhao, R. Su, Y. Huang, J. Wu, C. F. Fong, J. Feng, Q. Xiong, Transient circular dichroism and exciton spin dynamics in all-inorganic halide perovskites. *Nat. Commun.* **11**, 5665 (2020).

48. M. I. Dyakonov, V. I. Perel, Spin relaxation of conduction electrons in noncentrosymmetric semiconductors. *Sov. Phys. Solid State* **13**, 3023–3026 (1972).

49. Z. Chen, G. Dong, J. Qiu, Ultrafast pump-probe spectroscopy—A powerful tool for tracking spin-quantum dynamics in metal halide perovskites. *Adv. Quantum Technol.* **4**, 2100052 (2021).

50. J. Even, L. Pedesseau, M. A. Dupertuis, J. M. Jancu, C. Katan, Electronic model for self-as-sembled hybrid organic/perovskite semiconductors: Reverse band edge electronic states ordering and spin-orbit coupling. *Phys. Rev. B.* **86**, 205301 (2012).

51. L. Pedesseau, D. Sapori, B. Traore, R. Robles, H. H. Fang, M. A. Loi, W. Nie, J. C. Blancon, A. Neukirch, S. Tretiak, A. D. Mohite, C. Katan, J. Even, M. Kepenekian, Ad-vances and promises of layered halide hybrid perovskite semiconductors. *ACS Nano* **10**, 9776–9786 (2016).

52. Y. A. Bychkov, E. I. Rashba, Properties of a 2D electron gas with lifted spectral degeneracy. *JETP Lett.* **39**, 78–81 (1948).

53. M. Kepenekian, R. Robles, C. Katan, D. Sapori, L. Pedesseau, J. Even, Rashba and Dressel-haus effects in hybrid organic-inorganic perovskites: From basics to devices. *ACS Nano* **9**, 11557–11567 (2015).

54. B. Cheng, T. Y. Li, P. Maity, P. C. Wei, D. Nordlund, K. T. Ho, D. H. Lien, C. H. Lin, R. Z. Liang, X. Miao, I. A. Ajia, J. Yin, D. Sokaras, A. Javey, I. S. Roqan, O. F. Mohammed, J. H. He, Ex-tremely reduced dielectric confinement in two-dimensional hybrid perovskites with large polar organics. *Commun. Phys.* **1**, 80 (2018).

55. A. Ishii, T. Miyasaka, Direct detection of circular polarized light in helical 1D perovskite-based photodiode. *Sci. Adv.* **6**, eabd3274 (2020).

56. J. M. Soler, E. Artacho, J. D. Gale, A. García, J. Junquera, P. Ordejón, D. Sánchez-Portal, The SIESTA method for ab initio order-*N* materials simulation. *J. Phys. Condens. Matter* **14**, 2745–2779 (2002).

57. A. García, N. Papior, A. Akhtar, E. Artacho, V. Blum, E. Bosoni, P. Brandimarte, M. Brandbyge, J. I. Cerdá, F. Corsetti, R. Cuadrado, V. Dikan, J. Ferrer, J. Gale, P. García-Fernández, V. M. García-Suárez, S. García, G. Huhs, S. Illera, R. Korytár, P. Koval, I. Lebedeva, L. Lin, P. López-Tarifa, S. G. Mayo, S. Mohr, P. Ordejón, A. Postnikov, Y. Pouillon, M. Pruneda, R. Robles, D. Sánchez-Portal, J. M. Soler, R. Ullah, V. W. Z. Yu, J. Junquera, Siesta: Recent developments and applications. *J. Chem. Phys.* **152**, 204108 (2020).

58. M. Dion, H. Rydberg, E. Schröder, D. C. Langreth, B. I. Lundqvist, Van der Waals density functional for general geometries. *Phys. Rev. Lett.* **92**, 246401 (2004).

59. V. R. Cooper, Van der Waals density functional: An appropriate exchange functional. *Phys. Rev. B.* **81**, 161104 (2010).

60. R. Cuadrado, J. I. Cerdá, Fully relativistic pseudopotential formalism under an atomic orbital basis: Spin-orbit splittings and magnetic anisotropies. *J. Phys. Condens. Matter* **24**, 086005 (2012).

61. N. Troullier, J. L. Martins, Efficient pseudopotentials for plane-wave calculations. *Phys. Rev. B.* **43**, 1993–2006 (1991).

62. E. Artacho, D. Sánchez-Portal, P. Ordejón, A. García, J. M. Soler, Linear-scaling ab-initio calculations for large and complex systems. *Phys. Status Solidi B* **215**, 809–817 (1999).

63. J. C. de Mello, H. F. Wittmann, R. H. Friend, An improved experimental determination of external photoluminescence quantum efficiency. *Adv. Mater.* **9**, 230–232 (1997).

Science Advances

Bright circularly polarized photoluminescence in chiral layered hybrid lead-halide perovskites

Shangpu Liu, Mikaël Kepenekian, Stanislav Bodnar, Sascha Feldmann, Markus W. Heindl, Natalie Fehn, Jonathan Zerhoch, Andrii Shcherbakov, Alexander Pöthig, Yang Li, Ulrich W. Paetzold, Aras Kartouzian, Ian D. Sharp, Claudine Katan, Jacky Even, and Felix Deschler

View the article online
https://www.science.org/doi/10.1126/sciadv.adh5083
Permissions
https://www.science.org/help/reprints-and-permissions

Use of this article is subject to the Terms of service